Modeling compaction effects on the elastic properties of clay-water composites

Bernardo Moyano[1], Kyle T. Spikes[2], Tor Arne Johansen[1], and Nazmul Haque Mondol[3]

ABSTRACT

Modeling the elastic properties of clay-bearing rocks (shales) requires thorough knowledge of the mineral constituents, their elastic properties, pore space microstructure, and orientations of clay platelets. Information about these variables and their complex interrelationships is rarely available for real rocks. We theoretically modeled the elastic properties of synthetic clay-water composites compacted in the laboratory, including estimates of pore space topology and percolation behavior. The mineralogy of the samples was known exactly, and the focus was on two monomineralic samples comprised of kaolinite and smectite. We used differential effective medium theory (DEM) and analysis of scanning electron microscope (SEM) images of the compacted kaolinite and smectite samples. Percolation behavior was included through calculations of critical porosities from measurements of the liquid limits of the individual clay powders. Quantitative analysis of the SEM images showed that the large scale ($>0.1\ \mu m$) pore space of the smectite composite had more rounded pores (mean aspect ratio $\alpha = 0.55$) than the kaolinite composite (mean pore's aspect ratio $\alpha = 0.44$). However, models that used only these large-scale pore shapes could not explain the compressional and shear velocity measurements. DEM simulations with a single pore aspect ratio showed that bulk and shear moduli are controlled by different pore shapes. Conversely, modeling results that combined critical porosity and dual porosity models into DEM theory compared well with the measured bulk and shear moduli of compacting kaolinite and smectite composites. The methods and results we used could be used to model unconsolidated clay-bearing rocks of more complex mineralogy.

INTRODUCTION

Rock-physics modeling of the elastic properties of clay minerals under stress is of critical importance for the elastic characterization of shale rocks. Shales are composed primarily of silt-sized quartz and clay minerals, with kaolinite, smectite, and illite being the most abundant. Clay minerals characteristically have small grain sizes, plate-shaped grains, large surface area, and high cation-exchange capacity. However, their mechanical properties are not completely understood. The elastic properties of clay minerals are not well known, mainly because pure clay solid crystals (without pores) large enough to perform direct laboratory measurements are very rare in nature (Wang et al., 2001). Other sources of uncertainty in the rock-physics modeling of clay-bearing rocks arise from the pore space microstructure, orientation of platelets, and their geochemical interaction with pore fluids under burial stress. Understanding the mechanical compaction and elastic properties of clay-bearing rocks is important because they represent the most abundant infill of sedimentary basins, and they overlay most siliciclastic reservoirs. In addition, some organic-rich mudstones and shales have become reservoirs themselves although unconventional ones.

Estimates of elastic properties of clay minerals have been obtained using theoretical models (Katahara, 1996), combinations of experimental and theoretical studies (Wang et al., 2001), laboratory measurements on cold-pressed clay aggregates (Vanorio et al., 2003), extrapolations from laboratory measurements in shales (Han et al., 1986) and extrapolations from laboratory compacted clay-water composites (Mondol et al., 2008a). However, the results from those studies differ considerably. Theoretical computations produce much larger moduli ($k \sim 50$ GPa, $\mu \sim 20$ GPa) relative

to extrapolations from velocity measurements in shales or clay composites ($k \sim 20$ GPa, $\mu \sim 7$ GPa). In nature, clay minerals tend to adsorb water in their internal structures. This water can interact significantly with the clay, which can alter the effective elastic properties. Therefore, some authors propose rock-physics models for shales that use clay-water composites as a building unit of this type of rock (Hornby et al., 1994; Jakobsen et al., 2000; Johansen et al., 2004). Application of these models to natural shales requires extensive knowledge about volume fractions of all the constituents, their elastic properties, topology of pores and the orientation distribution function of clay platelets. Notably, the orientation of clay platelets, pore space microstructure and their evolution under increasing stress have been considered to control the degree of elastic anisotropy of shales.

In this work, we model fluid-saturated clay composites compacted in the laboratory at increasing effective pressure. Modeling synthetic composites, with mineralogy comprised of a single solid
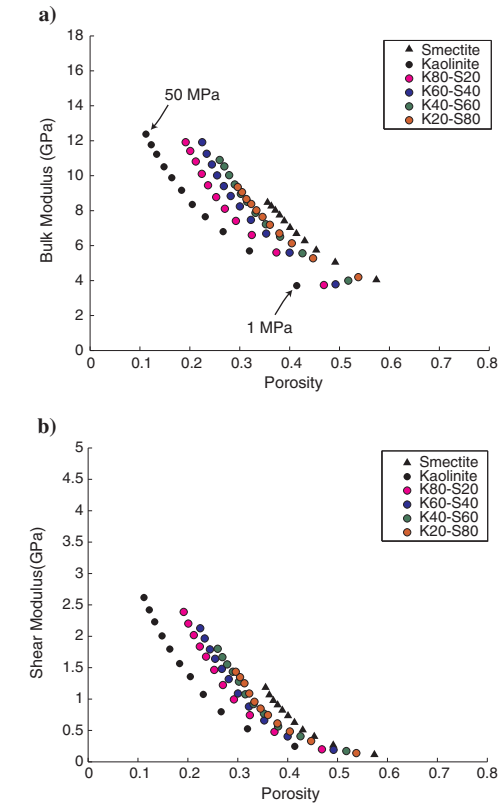

Figure 1. Bulk (a) and shear (b) moduli versus porosity for the 6 compacting clay-water composites used in this paper (modified from Mondol et al., 2007). Black circles are the kaolinite data and black triangle points the smectite data. Mixtures of both minerals are in colored circles. Clay fractions in weight percentage are indicated in the text box; K80-S20 means 80% kaolinite and 20% smectite mineral. The arrows indicate the initial (1 MPa) and final vertical effective stress (50 MPa) for the kaolinite sample.

phase such as kaolinite or smectite, is important because they provide unique conditions to understand the mechanical compaction of clay-bearing rocks and to estimate the elastic properties of clay minerals. The data measurements and experimental details have been published previously (Mondol et al., 2007, 2008a, 2008b). However, comprehensive effective medium modeling of the compressional and shear responses of the samples has not been completed. We used the isotropic formulation of differential effective medium (DEM) theory to model the monomineralic clay-water composites using single and multiple aspect ratio pore systems. The distribution of pore shapes was constrained by quantitative analysis of scanning electron microscopy (SEM) images of the compressed monomineralic samples. Then, we combined DEM with percolation behavior through an analogy with the concept of the "liquid limit" (Lagaly, 2006). This liquid limit is used to describe the plasticity of clay-fluid mixtures and engineering properties of fine-grained soils. Accordingly, laboratory measurements of monomineralic (kaolinite, smectite) composites and their mixtures were modeled combining critical porosity, SEM images analysis and bimodal distributions of aspect ratios. These results provided estimates of the elastic properties of the clay minerals. Similar modeling strategies could be applied to natural shale rocks, provided the necessary inputs can be obtained.

DATA SET

The data set modeled in this paper was collected at the Norwegian Geotechnical Institute (NGI). That experiment consisted of velocity measurements of uniaxial compaction of saturated (and dry) clay aggregates (Mondol et al., 2007). We modeled only the saturated samples. The composites were comprised of kaolinite, smectite, and a combination of both minerals. These minerals represent end members in terms of grain size and cation-exchange capacity. The particle sizes of the kaolinite were between 1 to 10 µm, whereas the smectite particles were smaller than 0.1 µm. The saturating fluid was sea water. Effective vertical stress varied at steps of approximately 5 to 50 MPa, from 1 to 50 MPa. Excess pore pressure was dissipated through drainage, and pore pressure was kept below 10% of the uniaxial vertical effective stress. P-wave and S-wave velocities were measured in the vertical direction. The resonant frequency of the transducers was 500 kHz. Porosity changes were calculated from the volume of expelled fluid. The measured velocities, the experimental set up, and sample preparation were reported opportunely in a series of papers (Mondol et al., 2007, 2008a, 2008b). The results of that experiment are summarized in Figure 1 in crossplots of elastic moduli versus porosity. In addition to the published data set, for our modeling we used SEM images of the single-mineral samples and measurements of the liquid limit of the clay powders. Both were collected by Mondol during the experimental work, but to date, they have not been published.

METHOD

DEM theory allows for computing the effective elastic properties of a two-phase composite by solving a coupled system of ordinary differential equations (Berryman, 1992),

$$(1-y)\frac{d}{dy}[K^*_{\text{DEM}}(y)] = (K_2 - K^*_{\text{DEM}})P^{(*2)}(y), \quad (1)$$

$$(1 - y) \frac{d}{dy} [\mu^*_{\text{DEM}}(y)] = (\mu_2 - \mu^*_{\text{DEM}}) Q^{(*2)}(y). \quad (2)$$

In equations 1 and 2, K^*_{DEM} and μ^*_{DEM} are the effective bulk and shear moduli, respectively, starting from initial conditions $K^*_{\text{DEM}}(0) = K_1$ and $\mu^*_{\text{DEM}}(0) = \mu_1$, which are usually set to the elastic moduli of the initial host material. The variables K_2 and μ_2 denote the moduli of the added inclusions, and the terms P^* and Q^* are geometrical factors associated with the inclusion material. Norris (1985) proves that DEM results are always between Hashin-Shtrikman bounds (Hashin and Shtrikman, 1963), but DEM models depend on the elastic properties of the constituents, the shape of the inclusions and the order in which they are added (i.e., the integration paths).

In a two-phase composite, DEM theory does not treat both phases equally. Instead, one material is considered a host into which inclusions of the second material are added in successive steps. In each step, the host material is replaced by the solution of the previous step. This procedure ensures that the host medium remains connected for the entire integration path. For a porous medium, this means that DEM with spherical inclusions predicts that the host (solid) material remains connected until 100% porosity. The final result also is path dependent, i.e., if the roles of host and inclusion materials are interchanged, then the calculated properties are different (Figure 2). A stiff solution is obtained when soft spherical inclusions are added to a stiff background medium (black solid lines in Figure 2). Counter to that, a soft solution results when stiff spherical inclusions are embedded within a soft background medium (black dashed lines in Figure 2).

However, the analysis above is only valid for spherical inclusions. If inclusions are oblate spheroids represented by an aspect ratio (ratio of minor to major axis) the DEM solution can be quite different. Integrating DEM equations from direct or reverse paths can produce stiff or soft composites depending on the elastic moduli of the constituents and the shape of the inclusions. For instance, a composite made of a soft matrix material with stiff inclusions can be stiffer than a stiff matrix with elongated compliant inclusions of the same shape (blue lines in Figure 2). This relates to the fact that elongated ellipsoidal inclusions are more efficient at softening and stiffening a host material than spherical inclusions.

In addition, for a two-phase composite DEM predicts critical thresholds at different porosities depending on the shape of the inclusions. Consider a calcite matrix into which water inclusions of a single aspect ratio are embedded in successive steps (Figure 3). The bulk modulus shows an asymptotic trend toward the suspension line, indicating that the host medium becomes disconnected at those threshold porosities (Figure 3a). For inclusions of different aspect ratios, DEM predicts that the shear modulus vanishes at different porosities (Figure 3b). These critical thresholds depend on the aspect ratios of the inclusions, and they are equal (or at least quite close) for bulk and shear moduli. Similar results are obtained for other solid materials. This modeling suggests that a geometric property is responsible for the connectivity of the included phase. At a given volume concentration, the phase 2 (fluid) becomes fully connected, shear modulus vanishes, and bulk modulus becomes that of a suspension. The numerical derivative of the bulk and shear moduli of the composite shows that the predicted threshold porosities are mainly controlled by aspect ratios of the inclusions (Figure 3c and 3d).

The effect of nonspherical inclusions in DEM theory is important because modeling clay-water composites may require the use of highly elongated inclusions to represent realistically the shape of pores and clay grains (aspect ratio $\sim 1/100$). The roles of host and inclusion materials also are important because these different shapes imply different microstructures. Starting from the mineral point (clay) and sequentially adding ellipsoidal fluid-filled inclusions implies a microstructure of a connected load-bearing clay phase. The elasticity of this medium is controlled by the number and shapes of fluid-filled pores. In contrast, integrating in the reverse path and sequentially embedding clay particles would emulate the effect of the number and shapes of clay grains in the elasticity of the medium. In the direct path, we model the effect of pore shapes; whereas in the reverse path, we emulate the effect of clay grain shapes on the elasticity of the medium.
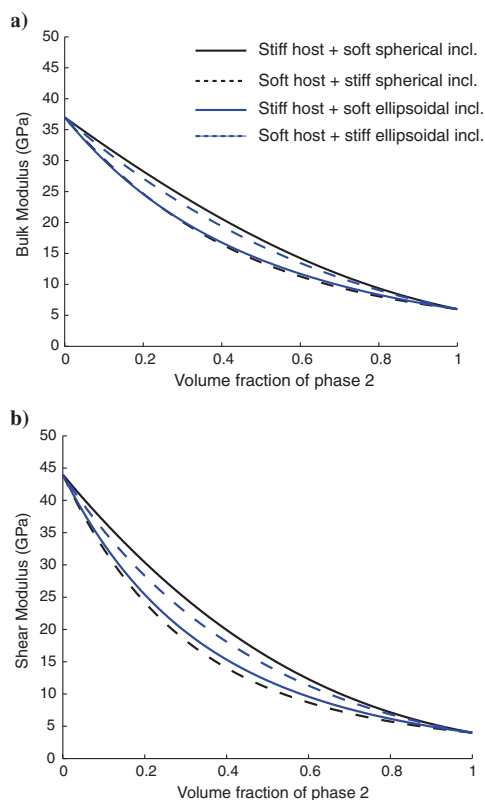

Figure 2. Comparison of effective bulk (a) and shear (b) modulus using DEM theory for a two-component composite of quartz ($k = 37$ GPa, $\mu = 44$ GPa) and smectite clay ($k = 6$ GPa, $\mu = 4$ GPa) using spherical (black lines) or spheroidal inclusions (blue lines) of aspect ratio 1/10 and integrating in both paths. The solid lines represent a stiff matrix with soft inclusions (direct path), whereas the dashed lines correspond to a soft matrix with stiff inclusions (reverse path). Note that elongated inclusions stiffen or soften a host material more efficiently than do spherical inclusions.

In general, laboratory acoustic sources create high-frequency conditions in which there is not enough time for wave-induced pore pressure increments to equilibrate. Therefore, we applied DEM theory with fluid-saturated inclusions, isolated with respect to fluid flow, to match the high-frequency conditions present in the laboratory.

The critical porosity and the critical phase

Analyses of natural sediments have demonstrated that a critical porosity (Φ_c) value exists, at which solid grains disconnect, shear resistance vanishes, and the mixture of solid and fluid behaves as a suspension. The critical porosity varies for rock types and separates two domains in the velocity-porosity plane. These include a domain where the rock is grain supported (solid) from another that is fluid supported or a suspension (Mavko et al., 2009). We mentioned previously that threshold porosities are predicted by DEM theory using nonspherical inclusions. Mukerji et al. (1995) propose another way of incorporating this behavior in the DEM scheme by redefining phase two (fluid) as a critical phase with finite effective properties (k_c, μ_c). They suggested that the moduli of the critical phase can be estimated by a Reuss (1929) average of end members or measured on loose sediments.

The concept of critical porosity and the use of a critical phase instead of pure fluid are particularly appealing in the modeling of clay aggregates. This is because the mechanical properties of clays can change when the clay mineral is in contact with a relatively small amount of water. These effective properties will differ from those of end-member or monomineralic clays. In soil mechanics and clay science, it is well known that depending on the water content, clay-water mixtures can behave as an elastic solid, as a fluid, or as a plastic solid (Lagaly, 2006). Clays with sufficient water content form slurries that behave as viscous fluids. If water content is reduced, eventually clay particles will bind to each other, and the mixture will behave as a plastic medium. The Atterberg limits (Lagaly, 2006) are well established empirical quantities, measureable in a laboratory, used to determine the transition points between those physical states. The liquid limit (LL) is the minimum amount of water at which the behavior of a clay-water mixture changes from plastic to liquid. The water content that separates the plastic and semisolid states is the plastic limit (PL). The difference between LL and PL is the plasticity index (PI), which is indicative of the plasticity of the clay. Montmorillonite, a member of the smectite group, is known to have a wide plasticity range indicated by a high PI (Lagaly, 2006).

The LL is defined as the minimum quantity of water (in weight percentage) required for the mass to begin flowing (Lagaly, 2006). This corresponds exactly with the critical porosity concept of porous rocks that separates two acoustic or mechanical domains. The only difference between Φ_c and LL is that LL is defined by a ratio of mass fractions (fluid/solid), whereas the Φ_c is a ratio of volume fractions (fluid/bulk). Fortunately, LL along with mass fractions and density of constituents (clays and fluid) were measured in laboratory for the data set used in this work. Accordingly, Φ_c was calculated for all the saturated samples using equations 3 and 4:

$$\Phi_c = \frac{V_{\text{bulk}} - V_{\text{solid}}}{V_{\text{bulk}}} = \frac{V_{\text{fluid}}}{V_{\text{clay}} + V_{\text{fluid}}}$$
$$= \frac{m_{\text{fluid}}/\rho_{\text{fluid}}}{\frac{m_{\text{clay}}}{\rho_{\text{clay}}} + \frac{m_{\text{fluid}}}{\rho_{\text{fluid}}}}, \tag{3}$$

$$LL = \frac{m_{\text{fluid}}}{m_{\text{clay}}}. \tag{4}$$

In these equations, V_{bulk} is the sample bulk volume, V_{clay} and V_{fluid} are volumes of clay and fluid, respectively, and they can be calculated from the corresponding mass (m_{fluid}, m_{clay}) fractions and densities (ρ_{fluid}, ρ_{clay}) for all the samples. The mass of the brine at the LL and the corresponding Φ_c were calculated using the densities and LL values measured for this data set (Mondol et al., 2008b). Those values for kaolinite, smectite, and brine are shown in Table 1. These critical porosity values correspond to this specific data set, made of particular kaolinite and smectite clay powders. However, it is worth mentioning that other laboratory studies on a kaolinite-water suspension (Vanorio et al., 2003) observed a change in P-wave quality factor and bulk modulus at very similar ranges of water content. More specifically, they mentioned a change in the slope of quality factor and bulk
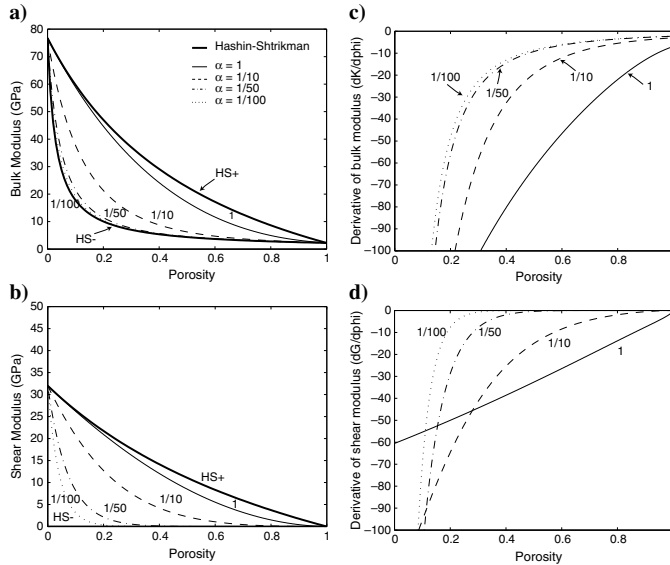
Figure 3. Effective bulk (a) and shear (b) moduli using DEM theory for a two-component composite of calcite and water, using single inclusions with aspect ratios of 1, 1/10, 1/50, and 1/100. Note that the shear modulus vanishes, and bulk modulus tends to a suspension at different porosity values for each aspect ratio. DEM model lines fall in between Hashin-Shtrikman bounds. Derivatives of bulk (c) and shear (d) moduli emphasize that the percolation porosities depend on the aspect ratios. Similar behavior is observed if the host material is quartz.

modulus at 0.4 of kaolinite content ($\Phi = 0.6$). Figure 7b in Vanorio et al. (2003) shows that the two slopes intersect at kaolinite content of 0.45 ($\Phi = 0.55$). This agrees very well with our calculation of the critical porosity ($\Phi_c = 0.56$) for a water-kaolinite sample. Moreover, Vanorio et al. (2003) measure the elastic modulus of the kaolinite-water mixture in that range of volume fractions. We can use those measurements as estimates of the elastic properties of the critical phase.

Clay minerals basic structures and associated pore space

Clay minerals are aluminosilicates with a sheet-like or layered structure. There are two basic units that form the sheets of clay minerals: The silicon tetrahedron (T) and the aluminum octahedron (O). These two units combine to form sheet structures. The T unit consists of 4 oxygen atoms surrounding silicon (SiO_4^{-4}) linked at the basal oxygen forming hexagonal sheets (Figure 4a). The apical oxygen point in the same direction and connect to other tetrahedral or octahedral sheets. Silicon can be partially replaced by other cations, such as Al^{+3} and Fe^{+3}. The O unit consists of an aluminum cation surrounded by six oxygen atoms (O^{-2}) or hydroxyls (OH^{-}) connected with other octahedra by sharing edges. Besides Al^{+2}, other common cations in the octahedron are Fe^{+3}, Mg^{+2}, and Fe^{+2} (Brigatti et al., 2006).

The tetrahedral sheet is always combined with an octahedral sheet. The stacking pattern of the layer sheet and the cation replacing silicon and aluminum determines the type of mineral formed. The main structural groups are the kaolin and smectite groups. Members of the kaolin group have a two layered structure (1:1) composed of one tetrahedral and one octahedral sheet. Kaolinite is by far the most abundant mineral in this group. In kaolinite, the distance between one silica layer and the next (basal distance) is 7Å (Figure 4b). A kaolinite particle may comprise over a hundred stacks of this ordered structure.

Minerals of the smectite group have a three-layered structure (1:2) with one alumina octahedral sheet located between two silica tetrahedral sheets (Figure 4b). Their typical basal spacing is approximately 14Å, but smectites can adsorb water molecules and expand their structure between 9Å (without water adsorbed) and 21Å (Tucker, 1991). Clay platelets tend to have a net surface charge, either attracting or repulsing other platelets.

In the following, we adopt the nomenclature for the different levels of organization of layers suggested by Bergaya and Lagaly (2006). A stack of several layers is referred to as a "particle" (cluster or domain), and an assembly of particles as an "aggregate." Accordingly, we distinguish three scales of pore space: (1) interlayer pores, between individual platelets, whose size and shape are similar to those of the layers themselves; (2) interparticle pores, between clay particles; and (3) interaggregate pores (Figure 5).

Table 1. Specimen details (Mondol et al., 2008b) and calculated critical porosities. The calculations used measurements of the liquid limits (LL$_{kaol}$ = 0.49, LL$_{smect}$ = 1.10), the densities (ρ_{kaol} = 2.616 g/cm^3, ρ_{smet} = 2.613 g/cm^3, ρ_{brine} = 1.025 g/cm^3) along with equations 3 and 4.

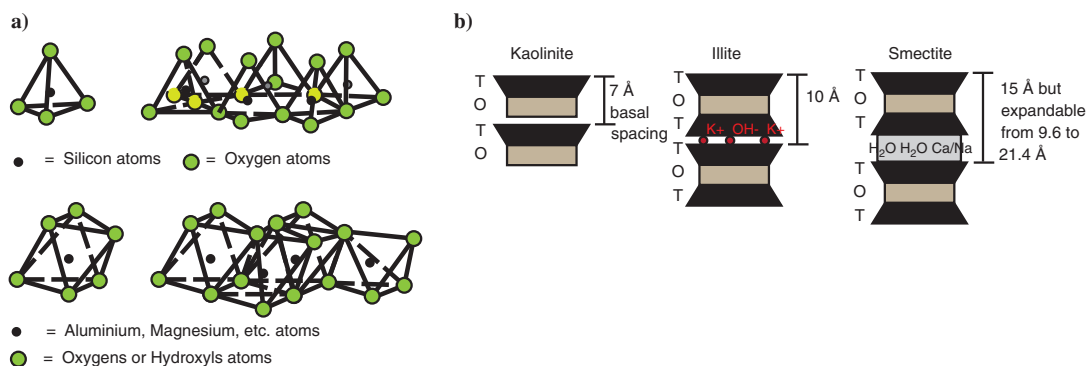| Clay fractions (wt%)		Mass of clays (g)		Critical porosity
Smectite	Kaolinite	Smectite	Kaolinite	
0	100	0	40.96	0.56
20	80	8.51	34.07	0.61
40	60	14.87	21.83	0.65
60	40	21.64	14.75	0.68
80	20	28.07	7.03	0.71
100	0	34.38	0	0.74

Figure 4. (a) Basic units of clay minerals: tetrahedron unit with one silicon and four oxygen atoms, and tetrahedral sheet; octahedron unit comprised of one aluminum and six oxygen or hydroxyl atoms, and octahedral sheet. (b) Basic groups of clay minerals according to the arrangements of sheets. Kaolin group has a two-layered (1:1) structure composed of one silica tetrahedral and one alumina octahedral sheet. The smectite group has a three-layered (1:2) structure comprised of one aluminum octahedral sheet between two silica tetrahedral sheets. Illite and smectite are common minerals of the second group. Modified from Tucker (1991).
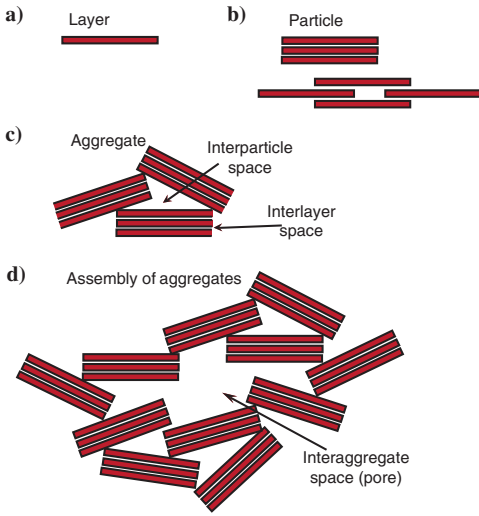
Figure 5. Arrangements of clay layer and associated pores: (a) clay mineral layer, (b) a particle comprised of a stack of layers, (c) an aggregate with interlayer and interparticle pore space, (d) an assembly of aggregates showing interaggregate pore space. Modified from Bergaya and Lagaly (2006).
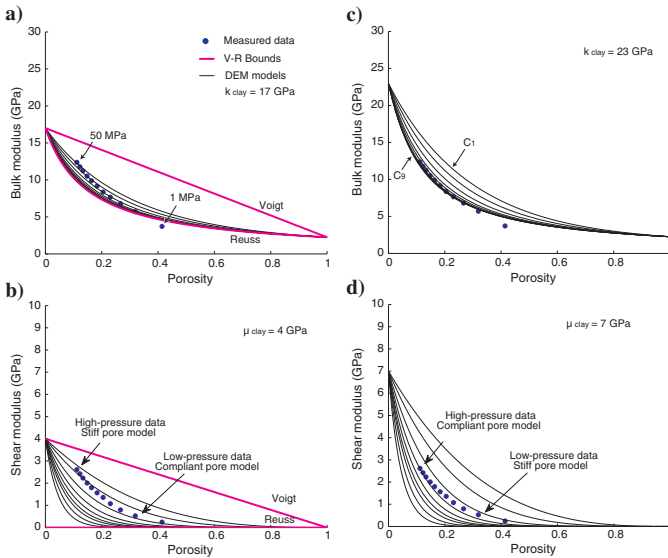

Figure 6. Bulk and shear moduli measurements versus porosity for a kaolinite-water composite, compared with DEM modelling for pore models as described in Table 2. Magenta lines are the Voigt-Reuss bounds; (a and b) show DEM modelling using minimum estimated elastic clay properties ($k = 17$ GPa and $\mu = 4$ GPa); (c and d) show DEM results using maximum estimated elastic properties ($k = 23$ GPa and $\mu = 7$ GPa). Note that for these values (c and d), the low-pressure data (high porosity) is modeled by a stiffer pore space than the high pressure data, which is not a valid representation of the mechanical compaction process.

MODELING COMPACTION EFFECTS ON CLAY-WATER COMPOSITES

During the uniaxial compression, the mechanical compaction of the clay-water composites reduced the porosities of the samples with a consequent increase in their effective elastic properties. We accounted for compaction effects through reduction of porosity in DEM theory, but we did not explicitly control pressure in the model formulation. This is a limitation of DEM. A number of other input parameters for the DEM modeling were recognized as unknown or uncertain. These include the elastic properties of the mineral constituents, the aspect ratios of the inclusions, and the elastic properties of a critical phase in terms of percolation behavior. Accordingly, the modeling of the experimental data requires a number of assumptions.

In the following subsections, we present different modeling strategies that successively reduce the number of unknowns. First, assuming that the compaction of the clay composites produces an overall stiffening of the pore space, we accounted for the pore-space stiffening by using multiple distributions of pore aspect ratios. Second, we performed DEM simulations, where aspect ratios were drawn from a uniform distribution. This was followed by inverting for the mostly likely aspect ratios. We repeated this but also included percolation behavior. Third, we analyzed SEM images of the compressed samples of pure kaolinite and pure smectite to estimate the topology of pores and grains. This image analysis led to using bimodal distributions of pore aspect ratios in the DEM modeling of the pure kaolinite, pure smectite, and finally, mixtures of the two.

DEM modeling using multiple distributions of pore aspect ratios

We first analyzed the data for the kaolinite-water composite, compacted from 1 to 50 MPa. Figure 6a and 6b shows a comparison of these data with theoretical bounds. The bounds were computed using clay mineral properties $k = 17$ GPa and $\mu = 4$ GPa and fluid bulk modulus $k_f = 2.25$ GPa. Noticeable first is the bulk modulus data point (at 1 MPa) that falls below the lower bound. This data point still fell beneath the suspension line (solid grains completely surrounded by fluid) computed using a very small mineral bulk modulus of 10 GPa. We attribute this to the difficulty of measuring P- and S-wave first arrivals on highly unconsolidated samples at such low effective pressures. Thus, we consider this measurement highly uncertain and focus our modeling on the higher pressure data.

We modeled the elastic properties of pure kaolinite using DEM theory with a pore space that included multiple aspect ratios (black lines in Figure 6a and 6b). In this case, kaolinite was considered the host material into which isolated ellipsoidal inclusions were embedded to obtain the target porosity. The kaolinite mineral properties ($k = 17$ GPa, $\mu = 4$ GPa) are slightly lower than those obtained by polynomial extrapolation of the

data and are considered a lower limit. The shapes of the fluid-filled oblate ellipsoids were defined by an arbitrary aspect ratio (α) distribution and an adherent volume concentration (C_i), both shown in Table 2. These distributions exhibit an overall weakening of the pore space from C_1 to C_9, indicated by a decrease in the concentration of stiff spherical pores ($\alpha = 1$) and an increase in concentration of compliant, low-aspect ratio pores. The uppermost line corresponds to C_1 and the lowermost to C_9. The model lines span the data for the bulk and shear moduli, but different models represent the two moduli. No individual model explains the data set completely. Models that include distributions with higher concentrations of compliant pores represent the high-porosity (low-pressure) data, whereas models that incorporate distributions with higher concentrations of stiff pores represent the low-porosity (high-pressure) data. The explanation is that the closing of compliant pores with increasing effective pressure results in a stiffer pore space at increasing pressure conditions.

Because the elastic properties of the kaolinite are not well known, we can repeat the modeling increasing the elastic moduli but only until a particular pair of values. At values of $k = 23$ GPa and $\mu = 7$ GPa, we fail to reproduce some of the bulk moduli data (Figure 6c), and we encounter a situation, more evident for the shear data, where models with a distribution of primarily compliant pores represent the high-pressure data (Figure 6d). This contradicts the assumption that the compaction of the composite produces a stiffening of the pore space. Thus, we consider these kaolinite properties as an upper limit when modeling the compaction with multiple distributions of pore aspect ratios. Appropriate elastic properties should be constrained to the obtained minimum and maximum values (17–23 GPa for bulk modulus and 4–7 GPa for shear modulus). The idealization of mechanical compaction by preferential closure of compliant pores allowed us to constrain the elastic properties of kaolinite. However, it fails to reproduce bulk and shear measurements by the same pore model. Yet, the modeling may be improved by using a different pore-shape distribution.

DEM simulations

In this section, we generated realizations of DEM models by drawing pore aspect ratios from a uniform distribution. The purpose was to identify a range of pore shapes that could model the data using elastic moduli between the limiting values determined in the previous section ($k = 17$–23 GPa, $\mu = 4$–7 GPa). We again focus on pure kaolinite as the host material. The aspect-ratio distribution was uniform with values ranging from highly elongated ($\alpha = 0.006$) to spherical pores ($\alpha = 1$). We generated 1500 realizations, where each realization included one pore shape for the entire modeled porosity range. This approach differs from the previous in which multiple pore shapes were used for a single DEM model. Figure 7a and 7b shows the 1500 simulations for bulk and shear moduli versus porosity (black lines) along with the laboratory data.

To determine which pore shapes provided the best fit to the data, we mapped the 100 closest values within a specified acceptance/rejection criterion. We extracted the corresponding aspect ratios from these best-match bulk and shear moduli, treating the moduli independently. Marginal probability distributions of aspect ratios were computed from these best-match values for each data measurement (Figure 7c and 7d). The most likely values of α for the bulk modulus

Table 2. Pore aspect ratio distribution and relative volume concentration in percentage (C_i) used in the DEM modeling.

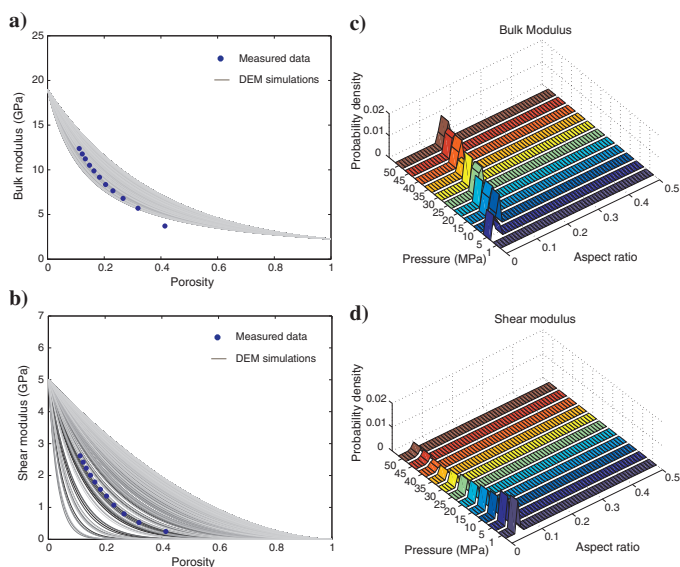| C_i = asp. ratio concentration distribution	α = Aspect ratio distribution			
	1	**0.1**	**0.01**	**0.001**
C_1	80	15	5	0
C_2	60	30	10	0
C_3	40	40	20	0
C_4	20	50	30	0
C_5	10	50	40	0
C_6	0	50	50	0
C_7	0	40	60	0
C_8	0	40	58	2
C_9	0	40	55	5

Figure 7. One thousand five hundred DEM simulations of bulk (a) and shear (b) moduli computed by drawing aspect ratios from a uniform distribution of range $\alpha = 0.006$–1. Mineral clay properties are $k = 19$ GPa and $\mu = 5$ GPa and fluid properties $k = 2.25$ GPa and $\mu = 0.0$ GPa. The closest model lines to the experimental data (blue points) are presented in 1D marginal probability distribution of aspect ratio for bulk (c) and shear (d) moduli. Shear data converge to $\alpha = 0.04$, whereas bulk modulus requires a range of $\alpha = 0.02$–0.15 for increasing pressure.

are from 0.02 to 0.15, with the smallest values corresponding to the lowest pressure. The shear modulus modeling converges to a unique most likely value of $\alpha = 0.04$. Different aspect ratios are required to model the bulk and shear moduli. An explanation is that the use of a fluid end member does not represent the situation. Accordingly, we repeat the simulations but include critical porosity and critical phase properties.

We model a mixture of pure kaolinite mineral with inclusions of a critical phase (Mukerji et al., 1995) at the critical porosity of $\Phi_c = 0.56$. This Φ_c was computed from the liquid limit measurement for the kaolinite sample (Table 1). Vanorio et al. (2003) measured a bulk modulus of $k = 3.02$ GPa in a kaolinite-water suspension for water content of 0.56, and we used this value for the bulk modulus of the critical phase in the DEM modeling. Using a uniform distribution of aspect ratios ($\alpha = 0.006–1$), 1500 simulations were generated; each simulation contains only one pore shape. Model lines and 1D marginal probability distributions are presented in Figure 8.

Notably, we found that for a given pair of clay mineral properties ($k = 22$ GPa and $\mu = 4.9$ GPa), DEM with critical porosity allows reproducing the bulk and shear moduli observations using a constant aspect ratio pore distribution for most of the measurements. The most likely aspect ratio are $\alpha = 0.3$ for bulk and $\alpha = 0.12$ for shear modulus for most of the porosity values. Exceptions

are the first pressure point (1 MPa, which we have already disregarded), and the next two pressure point (5 and 10 MPa), which required slightly wider distributions of aspect ratios. For these two pressures, the most likely aspect ratio reached $\alpha = 0.35$ for the bulk and $\alpha = 0.14$ for the shear modulus (Figure 8c and 8d). To model the shear stiffness, more elongated pores were required than for the bulk modulus. The latter seems to be controlled by more rounded or stiff pores. This implies that representing the pore distribution by a single aspect ratio might not be a satisfactory approximation for clay aggregates. One possible explanation is a bimodal distribution of pores shapes, in which the small aspect ratios would control the shear resistance, and large aspect ratios would dominate the incompressibility.

Description of the topology of pores from SEM images

We used two back-scattered electron images of the monomineralic samples after compaction to measure the pore space topology (Figures 9, 10, and 11). Our goal was to obtain estimates of the aspect ratios and orientations of pores. The image processing and analysis were done using ImageJ software (Rasband, 2011). Kaolinite and smectite images were oriented perpendicular to the direction of stress (i.e., the stress was applied along the vertical axis of the images). First, for the kaolinite sample (Figure 9a), a histogram of the intensity of the gray-scale image was computed. Second, a single threshold was selected to identify grains (gray) and pores (red), shown in Figure 9b. Third, the pore bodies were outlined (Figure 9c). Last, ellipses were fit to the pore outlines (Figure 9d). The aspect ratios of those ellipses were extracted, as well as the orientation angles of the ellipses. This angle is defined between the major axis of the ellipse and a line parallel to the horizontal image axis.

Selecting a threshold from an intensity histogram is not straightforward. This selection depends largely on the image resolution and the intensity contrast between pores and grains. It also is a key parameter when the objective is to estimate porosity based on the fractional 2D area of the image. In our case, the porosities of the samples were measured. Therefore, we used the measured porosities to guide the threshold selection such that the fractional 2D area (of pores) matched the observed porosity. Figure 10a displays the histogram of pore aspect ratios when the porosity is matched (blue). This histogram was modeled as a lognormal distribution with mean $x = 0.44$ and variance $\sigma = 0.041$ (red). The histogram of the orientation angle is displayed in blue in Figure 10b. It shows a slight but visible preferential orientation at approximately 40°. This was modeled with a gamma distribution.

To demonstrate that the threshold selection did not have a significant impact on the distribution of the pore aspect ratios, a second threshold was selected for comparison. This sensitivity analysis involved selecting the threshold such that the fractional 2D area was double (22%)
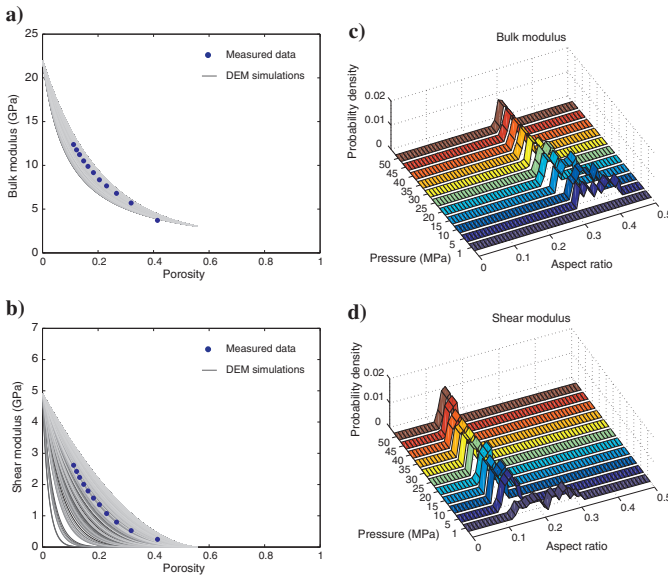

Figure 8. One thousand five hundred DEM simulations of bulk (a) and shear (b) moduli, drawing aspect ratios from a uniform distribution of range $\alpha = 0.006–1$, including the critical porosity concept. Clay properties are $k = 22$ GPa and $\mu = 4.9$ GPa, critical porosity is $\Phi_c = 0.56$, and critical phase bulk modulus is $k = 3.02$ GPa (measured by Vanorio et al.[2003]). The closest model lines to the measurements (blue points) are presented in 1D marginal probability distribution of aspect ratio for the bulk (c) and shear (d) moduli. Note that including critical porosity into DEM model reproduces bulk and shear moduli with constant aspect ratio distributions for the full range of pressures. These distributions are different for the bulk and shear moduli. Most likely values of aspect ratios are $\alpha = 0.3$ for the bulk and $\alpha = 0.12$ for shear modulus.

the measured porosity. The histograms for this trial for the aspect ratio and the orientation angle are in gray in Figure 10a and 10b, respectively. Quantile-quantile plots (Figure 10c and 10d) confirm that the distributions for the 11% and 22% porosity cases are quite similar, for the aspect ratios and angles.

The same image analysis procedure was performed on the pure smectite sample (Figure 11a and 11b). The pore aspect ratios in the smectite sample display a normal distribution with mean $x = 0.54$ and variance $\sigma = 0.035$ (Figure 11c). Orientation angles exhibit an approximate uniform distribution (Figure 11d).

The SEM images in Figures 9 and 11 provided information about large-scale pores. In each image the scale bar is 10 μm, and the minimum body analyzed was approximately 0.1 μm in size. Pores of this size are primarily interaggregate pores, with an accompanying small contribution of interparticle pore (between clusters). Interestingly, the kaolinite image (Figure 9a) showed platelets stacked together (as a deck of cards) forming particles or clusters with elongated pores between them. In contrast, the smectite image showed a honeycomb-like structure with fairly rounded pores without a predominant orientation (Figure 11a).

DEM modeling with a bimodal distribution of aspect ratios of pores

The distributions of aspect ratios obtained from the SEM analysis were used to constrain the pore shapes used in the DEM modeling. Specifically, these pore shapes represented the interaggregate and interparticle pores. However, the image analysis is at too large of a scale to observe the interlayer pores. We make the assumption that the pore space of the clay composites is a bimodal distribution of aspect ratios. One mode represents the shapes of large-scale pores, interaggregate and arguably some large interparticle pores. The second mode represents the shape of pores below the resolution of the available SEM images. They are pores at the scale of the clay particles, between the stacks of platelets. Their shapes are assumed to be similar to the individual grains. A recent study using SEM and atomic force microscopy measured the aspect ratio of kaolinite particles between 0.11 and 0.006, with a median of 0.022 (Gupta et al., 2011). Using these values for the shapes of the unseen pores, we model the kaolinite composite using DEM with a bimodal distribution of pore shapes as $\alpha_k = [0.02, 0.44]$ and an adherent concentration $c_k = [0.1, 0.9]$. The k subscript stands for kaolinite. This means that the pore space contains a 10% by volume of pores with aspect ratio $\alpha = 0.02$ and 90% with $\alpha = 0.44$.
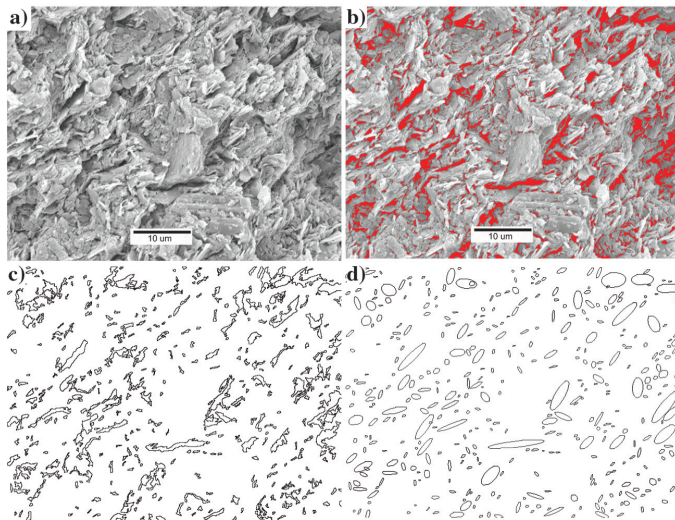

Figure 9. (a) SEM image of fluid-saturated kaolinite used to estimate the pore shapes. (b) The same image segmented into pores and clay matrix. (c) Outlines of the extracted pores and (d) ellipses used for the estimations of pore aspect ratios. The scale bar in (a) and b) is 10 μm. The proportional 2D area occupied by the pores is 11%.
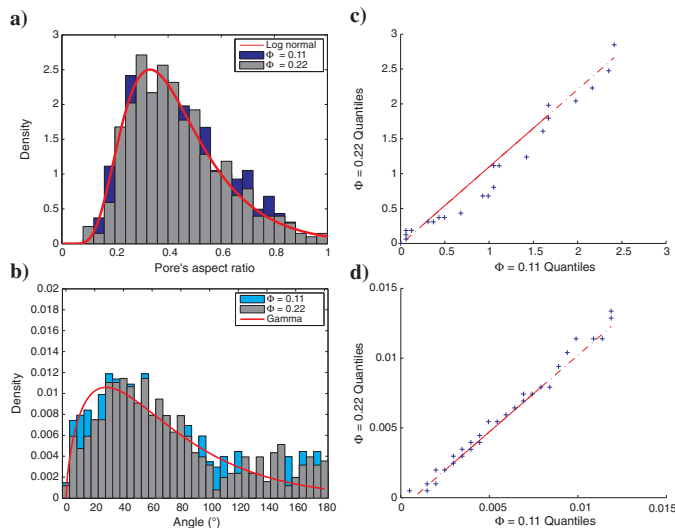

Figure 10. Sensitivity analyses of the change in pore aspect ratio (a) for the kaolinite sample and orientation distributions (b) calculated from segmented images using two different threshold values. One value is such that the 2D proportional area matches the porosity of the sample (11%) and the other is twice that value (22%). Quantile-quantile plots of both aspect ratio distributions (c) and orientation angle distributions (d) indicate the similarity between the distributions. A one-to-one line is drawn between the first and third quantiles.
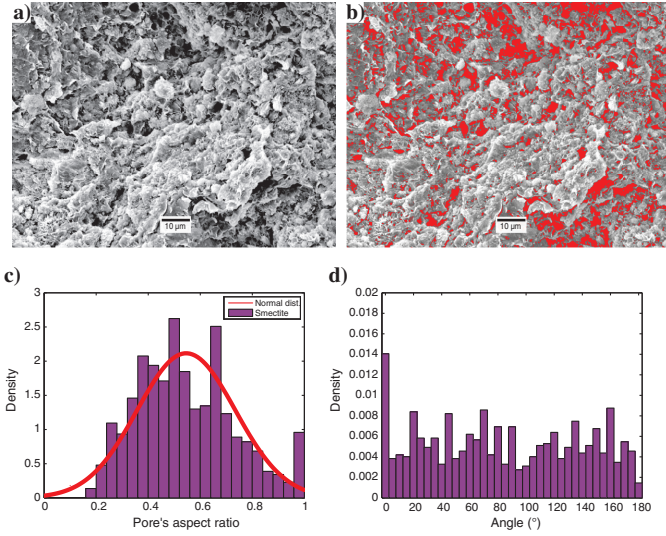
Figure 11. (a) Smectite SEM image, (b) segmented image, (c) pore aspect ratio distribution, and (d) orientation angle distribution. Pores in the smectite sample are more rounded than those of the kaolinite (compare with Figure 9a), and they lack of apparent preferential orientation. Note the honeycomb structure of the grains in the pure smectite sample. The scale bar in (a and b) indicate 10 μm.

The pore space of the smectite sample also was represented by a bimodal distribution as $\alpha_s = [0.01, 0.55]$ and a concentration distribution $c_s = [0.1, 0.9]$, where the s subscript is for smectite. The stiff mode of the distribution came from the normal distribution in Figure 11c. The small-scale pore shapes were based on small angle neutron scattering studies of synthetic smectite by Knudsen et al. (2003) who proposed that individual grains can be as much as 100 times larger in lateral dimension than in thickness.

Finally, critical porosities for smectite and kaolinite samples were computed from liquid limit measurements (Table 1). Bulk modulus values of the critical phase were taken from Vanorio et al. (2003) for kaolinite and computed by the Reuss average of fluid ($k = 2.25$ GPa) and $k = 36$ GPa for the smectite sample. Figure 12 compares the data measurements with the DEM modeling. The elastic moduli used were $k = 22$ GPa and $\mu = 4.9$ GPa for the kaolinite data. The smectite elastic properties were $k = 36$ GPa and $\mu = 14$ GPa. The combination of critical porosity and a bimodal pore distribution matched the measurements of elastic moduli with residuals (differences between predicted and observed data) less than 0.5 GPa for kaolinite and smectite data sets. The root-mean-square (rms) deviations were $k_{rms} = 0.0168$ GPa and $\mu_{rms} = 0.0014$ GPa for the kaolinite data and $k_{rms} = 0.02$ GPa and $\mu_{rms} = 0.0004$ GPa for the smectite data.

Modeling mixtures of clay minerals (kaolinite-smectite aggregates)

To model the compaction of samples that consisted of mixtures of kaolinite and smectite, we used the parameters obtained in the previous section. Mineral elastic properties were calculated by the Voigt average of the estimated pure kaolinite elastic properties ($k = 22$ GPa, $\mu = 4.9$ GPa) and smectite properties ($k = 36$ GPa, $\mu = 14$ GPa). Critical phase properties were calculated by the Voigt average of individual phases used in the section above. The critical porosities were calculated from liquid limit measurements (Table 1). The pore distribution was constructed by combining the bimodal distribution of the end member lithologies, i.e., $\alpha = [(0.02, 0.44), (0.01, 0.55)]$, with concentrations as defined in the volume fractions of each mineral in the sample. For instance a composite made of 80% kaolinite and 20% smectite mineral had a distribution of aspect ratios $\alpha = [(0.02, 0.44), (0.01, 0.55)]$ with an adherent concentration of $c = [(0.1, 0.9) * 0.8, (0.1, 0.9) * 0.2]$.

Figure 13 shows modeling results along with the data measurements. The DEM model lines, representing an effective medium, follow fairly
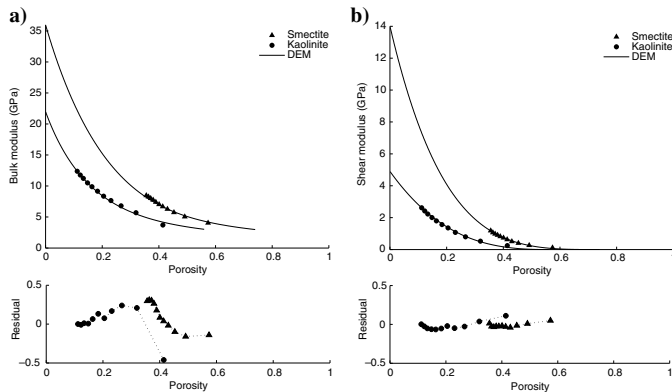

Figure 12. DEM modeling and residuals of bulk (a) and shear (b) elastic moduli using a bimodal distribution of aspect ratio of pores. Circles are the kaolinite data and triangle points the smectite data. Kaolinite mineral properties are $k = 22$ GPa and $\mu = 4.9$ GPa, critical porosity $\Phi_c = 0.56$, critical phase properties $k = 3.02$ GPa (Vanorio et al., 2003), and $\mu = 0.0$ GPa. Pore aspect ratios are $\alpha = [0.02, 0.44]$ with a concentration of $c = [0.1, 0.9]$. Smectite mineral properties are $k = 36$ GPA and $\mu = 14$ GPa, pore's aspect ratios $\alpha = [0.01, 0.55]$ with a corresponding concentration of $c = [0.1, 0.9]$. Smectite critical porosity is $\Phi_c = 0.74$ and elastic properties of the critical phase were computed by the Reuss average of fluid ($k = 2.25$ GPa) and smectite ($k = 36$ GPa). Model residual errors are less than 0.5 GPa for both moduli and both kaolinite and smectite data sets.

parallel trends, whereas some data measurements show intersecting trends. Specifically, the composites with smectite content greater than 60% show some overlap (orange and green points). The reason for this can be that the mixtures of clay minerals are not statistically homogeneous composites. A statistically homogeneous medium is heterogeneous at a relatively small scale but appears homogeneous on a larger scale. This underlines the application of an effective medium theory (Gueguen and Palciauskas, 1994). Instead, the samples may be aggregates of clusters of the individual lithologies. An alternative strategy to model the mixtures of clay minerals considering clusters of both lithologies and their different compaction rates have been proposed by Jensen et al. (2011).

DISCUSSION

A thorough analysis of the anisotropy of the samples under compaction was not possible because for this data set, velocities were measured only in the vertical direction. However, we can speculate about a plausible anisotropic character of the samples by analyzing the initial particle orientation and its evolution under increasing vertical stress. A partial orientation of plate-like particles can exist, and it would increase with increasing vertical stress. In fact, our analysis of interaggregate pores in the kaolinite sample showed a slight but visible preferential orientation (Figures 9 and 10). This degree of orientation of pores appears relatively small to produce a strong anisotropic effect. In contrast, the smectite SEM image showed quite rounded pores without a preferential orientation (Figure 11). Its microstructure resembles a honeycomb structure without a dominant alignment of pores or clay particles. These observations agree well with measurements on similar samples performed by Holt et al. (2011) who find that initial P-wave anisotropy was larger for a kaolinite ($\varepsilon < 0.1$) than for a smectite sample ($\varepsilon \sim 0.02$). They also observe that the anisotropy of the kaolinite sample did not vary significantly with stress, whereas the smectite sample's anisotropy slightly increased with net stress. The SEM images analyzed in our study were captured after the compaction experiment, and they represent the final conditions of the microstructure. Therefore, the degree of P-wave anisotropy of the samples seems not as high as it might be expected for these lithologies. This could partially explain the success of an isotropic DEM modeling reproducing the observations.

Other reasons for the apparent isotropic character of the composites can be related to their preparation and experimental setups. These samples were made of clay powder and sea water mixed in slurries, under continuous stirring and shaking to ensure a homogeneous mixture of the components, to avoid air being trapped and clumps formed. In such conditions, layering and a strong orientation of clay platelets seems unlikely. In fact, continuous stirring and shaking would tend to create a random orientation of particles and an isotropic sample. Besides, the compaction experiment is restricted only to vertical strains. The walls of the cylinder do not allow lateral strains, fostering volume reduction by pore space (fluid) reduction (expulsion) and restricting the reorientation of clay platelets.

DEM theory requires the addition of inclusions of a material (fluid), normally described by one shape parameter such as aspect ratio, in a host medium of another material (clay mineral). However, in clay-bearing rocks, there may be pores of several sizes and shapes. Recent studies (Kuila and Prasad, 2011) observe bimodal distributions of pore sizes in montmorillonite samples (smectite)

and primarily unimodal distributions in kaolinite samples. In our DEM modeling of the kaolinite composite, we were unable to reproduce both measurements of bulk and shear moduli with the aspect ratio calculated from the SEM images ($\alpha = 0.44$). Including a small volume (10%) of pores with an aspect ratio similar to that of kaolinite grains ($\alpha = 0.02$) significantly improved the modeling of bulk and shear moduli. Similarly, for the smectite data, considering the aspect ratio of interaggregate pores observed in the SEM images ($\alpha = 0.55$) and a small volume of aspect ratio on the order of smectite individual platelets ($\alpha = 0.01$) allowed to reproduce bulk and shear moduli observations. Nevertheless, the volume concentration of those small scale pore shapes is difficult to estimate. Their contribution to the total porosity is not expected to be high, but pure clay mineral samples such as those studied here might have a concentration greater than 10%.
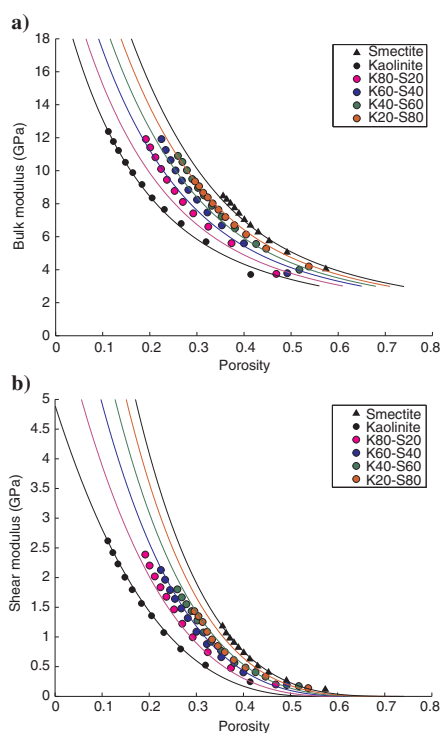

Figure 13. DEM modeling of bulk (a) and shear (b) elastic moduli of the compaction of clay composites constituted of kaolinite, smectite, and four mixtures. Elastic properties of the mixtures of clay minerals were calculated by the Voigt average of individual mineral phases. Critical porosities were calculated from liquid limit measurements (Table 1). Elastic properties of critical phases were calculated by the Voigt average of the properties used for single mineral samples. Clay fractions in weight percentage are as indicated in the text box; "K80-S20" means 80% kaolinite and 20% smectite mineral. Aspect ratio distributions of pores are the combined bimodal distribution of end-member lithologies, $\alpha = [(0.02, 0.44), (0.01, 0.55)]$, with the corresponding concentration according to the relative concentration of each clay mineral.

The DEM simulations (and inversion) with single aspect ratio of the kaolinite composite showed a fair match of each elastic modulus separately, i.e., obtaining different aspect ratios for bulk and shear modulus (Figure 8). This suggest that replacing the pore space structure by a single (effective) aspect ratio might be valid when only one elastic modulus is analyzed. But it becomes inconsistent when bulk and shear moduli are considered because they seem to be controlled by different parts of the aspect ratio distribution.

We observed that the sensitivities of the modeled bulk and shear moduli to pore shapes are quite different. A minor percentage of inclusions of very low aspect ratio significantly decrease the shear resistance but negligibly affects the incompressibility of the effective medium. This implies that highly elongated pores, under shear stress represent important planes for shear failure. However, they may not be compliant under compressive stress.

The samples modeled were composed of clay powder and sea water. However, in our modeling we used pure water properties ($k = 2.25$ GPa, $\mu = 0$ GPa) and critical phase properties obtained from the work of Vanorio et al. (2003). Although our approach was mainly micromechanical, we assumed that any effect on the elastic properties of the fluid phase due to salinity or chemical interactions between clay and water (if any) would be accounted for on the properties of the critical phase. In addition, smectites have high surface area, high cation-exchange capacity, and they can swell when in contact with fluids. Swelling and expansion of the sample in the closed system in which the acoustic measurements were acquired seems unlikely. A thorough assessment of the level of interaction between solid and fluid phases would require comparison of chemical composition of mixing and expelled fluid. The lack of such measurements on the samples studied prevents further analysis of those aspects and represents an additional source of uncertainty for the micromechanical modeling proposed here.

CONCLUSIONS

We modeled the compaction of saturated synthetic clay composites using differential effective medium theory. Our aim was to determine if the mechanical compaction of fluid-saturated clay composites can be reproduced by a micromechanical model accounting for the microstructure of the pores and clay platelets. The modeling included the analysis of SEM images of the microstructure of the compacted samples. This revealed that the pore space of the smectite sample was composed of quite rounded and stiff pores (mean aspect ratio $\alpha = 0.55$), whereas the kaolinite pore topology was dominated by more elongated and compliant pores (mean $\alpha = 0.44$). For this reason, kaolinite samples might be more anisotropic than smectite samples.

Simulations using single-pore shapes indicated that bulk and shear moduli were controlled by different aspect ratios. Bulk modulus measurements were dominated by stiff pores (large α), whereas shear data were controlled by more elongated pores (small α). This, combined with the analysis of SEM images, suggested that the elastic properties of the clay-bearing rocks are influenced by pores of different sizes. The large-scale pores (interaggregates) can be analyzed by SEM images, whereas the small-scale pores are similar in size and shape to the clay platelets.

Percolation behavior was observed, and critical porosity values were calculated from measurements of liquid limits of the kaolinite and smectite powders. The estimations agreed well with laboratory

studies of acoustic properties of kaolinite-water suspension. Combining critical porosity, elastic properties of a critical phase and bimodal aspect ratio pore space into differential effective medium theory compared well with the velocity measurements of pure clay composites and their mixtures for the studied pressure conditions. The analysis of SEM images and the success of the isotropic modeling suggest that the anisotropy of these synthetic clay composites would not be as high as it might be expected for this kind of lithology.

ACKNOWLEDGMENTS

REFERENCES

Bergaya, F., and G. Lagaly, 2006, General introduction: Clays, clay minerals, and clay science, *in* F. Bergaya, B. K. G. Theng, and G. Lagaly, eds., Handbook of clay science: Elsevier.

Berryman, J. G., 1992, Single-scattering approximations for coefficients in Biot equations of poroelasticity: Journal of the Acoustical Society of America, **91**, 551–571, doi: 10.1121/1.402518.

Brigatti, M. F., E. Galan, and B. K. G. Theng, 2006, Structures and mineralogy of clay minerals, *in* F. Bergaya, B. K. G. Theng, and G. Lagaly, eds., Handbook of clay science: Elsevier.

Gueguen, Y., and V. Palciauskas, 1994, Introduction to the physics of rocks: Princeton University Press.

Gupta, V., M. A. Hampton, J. R. Stokes, A. V. Nguyen, and J. D. Miller, 2011, Particle interactions in kaolinite suspensions and corresponding aggregate structures: Journal of Colloid and Interface Science, **359**, 95–103, doi: 10.1016/j.jcis.2011.03.043.

Han, D.-H., A. Nur, and D. Morgan, 1986, Effects of porosity and clay content on wave velocities in sandstones: Geophysics, **51**, 2093–2107, doi: 10.1190/1.1442062.

Hashin, Z., and S. Shtrikman, 1963, A variational approach to the theory of the elastic behaviour of multiphase materials: Journal of the Mechanics and Physics of Solids, **11**, 127–140, doi: 10.1016/0022-5096(63)90060-7.

Holt, R., M. Bhuiyan, M. Kolstø, A. Bakk, J. Stenebråten, and E. Fjer, 2011, Stress-induced versus lithological anisotropy in compacted claystones and soft shales: The Leading Edge, **30**, 312–317, doi: 10.1190/1.3567262.

Hornby, B. E., L. M. Schwartz, and J. A. Hudson, 1994, Anisotropic effective-medium modeling of the elastic properties of shales: Geophysics, **59**, 1570–1583, doi: 10.1190/1.1443546.

Jakobsen, M., J. A. Hudson, T. A. Minshull, and S. C. Singh, 2000, Elastic properties of hydrate-bearing sediments using effective medium theory: Journal of Geophysical Research Solid Earth, **105**, 561–577, doi: 10.1029/1999JB900190.

Jensen, E. H., C. F. Andersen, and T. A. Johansen, 2011, Estimation of elastic moduli of mixed porous clay composites: Geophysics, **76**, no. 1, E9–E20, doi: 10.1190/1.3511351.

Johansen, T. A., B. O. Ruud, and M. Jakobsen, 2004, Effect of grain scale alignment on seismic anisotropy and reflectivity of shales: Geophysical Prospecting, **52**, 133–149, doi: 10.1046/j.1365-2478.2003.00405.x.

Katahara, K. W., 1996, Clay mineral elastic properties: 66th Annual International Meeting, SEG, Expanded Abstracts, 1691–1694.

Knudsen, K. D., J. O. Fossum, G. Helgesen, and V. Bergaplass, 2003, Pore characteristics and water absorption in a synthetic smectite clay: Journal of Applied Crystallography, **36**, 587–591, doi: 10.1107/S0021889803001778.

Kuila, U., and M. Prasad, 2011, Surface area and pore-size distribution in clays and shales: Society of Petroleum Engineers Annual Technical Conference, SPE 146869.

Lagaly, G., 2006, Colloid clay science, *in* F. Bergaya, B. K. G. Theng, and G. Lagaly, eds., Handbook of clay science: Elsevier.

Mavko, G., T. Mukerji, and J. Dvorkin, 2009, The rock physics handbook: Tools for seismic analysis of porous media, 2nd ed.: Cambridge University Press.

Mondol, N. H., K. Bjorlykke, and J. Jahren, 2008b, Experimental compaction of clays: Relationship between permeability and petrophysical properties in mudstones: Petroleum Geoscience, **14**, 319–337, doi: 10.1144/1354-079308-773.

Mondol, N. H., K. Bjorlykke, J. Jahren, and K. Hoeg, 2007, Experimental mechanical compaction of clay mineral aggregates — Changes in physical

properties of mudstones during burial: Marine and Petroleum Geology, **24**, 289–311, doi: 10.1016/j.marpetgeo.2007.03.006.

Mondol, N. H., J. Jahren, K. Bjorlykke, and I. Brevik, 2008a, Elastic properties of clay minerals: The Leading Edge, **27**, 758–770, doi: 10.1190/1.2944163.

Mukerji, T., J. Berryman, G. Mavko, and P. Berge, 1995, Differential effective-medium modeling of rock elastic-moduli with critical porosity constraints: Geophysical Research Letters, **22**, 555–558, doi: 10.1029/95GL00164.

Norris, A., 1985, A differential scheme for the effective moduli of composites: Mechanics of Materials, **4**, 1–16, doi: 10.1016/0167-6636(85)90002-X.

Rasband, W. S., 2011, ImageJ: U. S. National Institutes of Health, Bethesda.

Reuss, A., 1929, Account of the liquid limit of mixed crystals on the basis of the plasticity condition for single crystal: Zeitschrift fur Angewandte Mathematik und Mechanik, **9**, 49–58.

Tucker, M. E., 1991, Sedimentary petrology: An introduction to the origin of sedimentary rocks: Blackwell Scientific Publications.

Vanorio, T., M. Prasad, and A. Nur, 2003, Elastic properties of dry clay mineral aggregates, suspensions and sandstones: Geophysical Journal International, **155**, 319–326, doi: 10.1046/j.1365-246X.2003.02046.x.

Wang, Z. J., H. Wang, and M. E. Cates, 2001, Effective elastic properties of solid clays: Geophysics, **66**, 428–440, doi: 10.1190/1.1444934.